No Bridge Between Us: Two Distant Iron Ions Comprise the Active Site of Alkane Monooxygenase (AlkB)

Clorice R. Reinhardt[1], Juliet A. Lee[2†], Lauren Hendricks[2†], Tierani Green[2†], Lily Kunczynski[2], August Jaunzarins Roberts[2], Naomi Miller[2], Noga Rafalin[2], Heather J. Kulik[1,3], Christopher J. Pollock*[4], Rachel N Austin*[2]

[1]Department of Chemical Engineering, Massachusetts Institute of Technology, Cambridge, MA 02139, USA

[2]Department of Chemistry, Barnard College, 3009 Broadway, NY 10027 USA

[3]Department of Chemistry, Massachusetts Institute of Technology, Cambridge, MA 02139, USA

[4]Cornell High Energy Synchrotron Source, Wilson Laboratory, Cornell University, Ithaca, NY 14853, USA

ABSTRACT: Alkane monooxygenase (AlkB) is the dominant enzyme that catalyzes the oxidation of liquid alkanes in the environment. Two recent structural models derived from cryo-electron microscopy (cryo-EM) data make visible numerous attributes of the enzyme that had previously been the source of speculation. The structure of the diiron active site is unusual: a histidine-rich center that binds two iron ions without a bridging ligand. This finding makes it difficult to understand how the iron ions coordinate oxidation state changes to achieve the high-valent conditions presumed necessary to activate strong C-H bonds. To ensure that potential photoreduction and radiation damage are not responsible for the absence of a bridging ligand in the resting state cryo-EM structures, spectroscopic methods are needed. We present the results of extended x-ray absorption fine structure (EXAFS) experiments collected under conditions where photodamage was avoided. Careful data analysis reveals an active site structure consistent with the cryo-EM structures in which the two iron ions are ligated by nine histidines and are separated by at least 5 Å. The EXAFS data were used to inform structural models for molecular dynamics (MD) simulations. The MD simulations corroborate EXAFS observations that neither of the two key carboxylate-containing residues (E281 and D190) are likely candidates for metal ion bridging. To further explore the role of these carboxylate residues, we used mutagenesis experiments, spectroscopy, and additional MD simulations to understand the role of these residues. A variant in which a carboxylate containing residue (E281) was changed to a methyl residue (E281A) showed little change in pre-edge features, consistent with the observation that it is not essential for activity and hence unlikely to serve as a bridging ligand at any point in the catalytic cycle. D190 variants had substantially diminished activity, suggesting an important role in catalysis not yet fully understood.

INTRODUCTION

Alkane monooxygenase (AlkB) is an integral membrane metalloenzyme thought to be responsible for catalyzing the oxidation of medium chain length linear alkanes in the environment.[1-14] First identified and partially purified in the late 1960s[15], it was gradually recognized as a member of the class-III diiron proteins, along with membrane spanning fatty acid desaturases, fatty acid hydroxylases, xylene monooxygenase, UndB, C-4 methyl sterol oxidase, and β-carotene ketolase.[16-23] Key studies over the ensuing decades mapped the substrate scope of the enzyme, which favors terminal hydroxylation or epoxidation of straight chain alkanes or alkenes with limited tolerance for cyclic alkanes.[24-30]

For more than 50 years, the tertiary structure of AlkB was not known. However, in early 2023, two cryo-electron microscopy (cryo-EM) structures of two different AlkBs, both from the organism *F. thermophila*, were published.[31, 32] The two structures are remarkably similar. Both show the six predicted trans-membrane helices with a substrate channel leading from the periplasmic side of the protein to the active site, which rests in the cytoplasmic side of the membrane. The active site is comprised of two iron ions, coordinated by a total of nine

histidines in a pseudo-octahedral geometry. The two iron ions are separated by more than 5 Å with no covalent connection between them. This active site is similar to the active site of the two other class-III diiron proteins, stearoyl coA desaturase (SCD) and fatty acid hydroxylase (FA2H) whose structures have recently been solved, and make clear that the active site of the class-III diiron proteins is quite different from the canonical, and better characterized, soluble diiron proteins like soluble methane monooxygenase and toluene monooxygenase.[33-37]

Several explanations have been offered for how the novel active site structure catalyzes the oxidation of alkanes. Chai *et al.* suggested that once the protein is reduced, and oxygen binds and is cleaved, a high valent intermediate with an Fe(IV)-Fe(IV)-O_2 diamond core forms.[31] While a reasonable *a priori* hypothesis, sufficient data is still not available to predict how this structural rearrangement occurs.[31] An earlier EXAFS paper, while acknowledging the complexity of the data it reported, concluded that the active site of AlkB likely contains a short (3.1 Å) Fe-Fe distance.[38] Such a short distance is not visible in either of the AlkB structures, nor in any of the four structures of other structurally characterized members of the class-III diiron proteins.[33-35, 39] However, it is possible under conditions less damaging than those of cryo-EM or X-ray crystallography that a short iron-iron distance would be apparent. Alternatively, the high-valent chemistry may reside on only one of the two iron ions, with the other iron ion serving as a shuttle for protons and electrons.[32, 40]

A short iron-iron distance would require that a ligand bridge the two highly charged ions.[41] Such a role could be filled by a nearby carboxylate, such as D181 in *Pseudomonas putida* (Pp). When this residue was changed to an A, the resulting variant was inactive,[17] though in both cryo-EM structures this residue is not within bonding distance of either iron ion. However, these confounding results are not completely unprecedented. A recent paper on plasmanylethanolamine desaturase (PEDS1) that screened all conserved residues in the fatty acid desaturase family, found that only one residue, an aspartate, was essential for activity.[42] Using homology modeling and AlphaFold2, they predicted that its function was to hydrogen bond to one of the ligating histidines and stabilize the bound iron, which might be relevant in understanding the importance of PpD181.[43] Both structures have another carboxylic acid containing residue (FtE281 or FtAlkBGE271 in AlkBG, where "BG" indicates that this cryo-EM structures is of a two domain AlkB in which the rubredoxin domain (G) is covalently bound) that is much closer to the active site than PpD181/FtD190. We showed previously that FtE281A is active, an observation inconsistent with it being an essential bridging ligand during the catalytic cycle.[32]

We speculated, prior to determining the structure of AlkB, that an imidazolate could bridge the two iron ions. Such a geometry is found in Cu Zn superoxide dismutase.[44-46] A ferrous metal-organic framework with bridging imidazolates has an iron-iron distance of 6.1 Å.[47] No such bridging imidazolate, however, is present in any of the structures of class-III diiron enzymes and the iron-iron distance in FtAlkB (5.4 Å) is likely too short to be held together in this fashion.

Another candidate for a bridging ligand would be an oxo or hydroxo moiety. A previously published Mössbauer study concluded, based on the estimated strong antiparallel coupling ($J > 80$ cm^{-1}) between the two iron ions, that they were most likely linked by an oxo bridge.[16] Electron paramagnetic resonance (EPR) data described, but not shown, in that work was also consistent with an antiparallel coupled ground state, energetically well separated from the nearest excited state.[16] Notably, none of the published structures show an oxo or hydroxo bridge, and even the prior published EXAFS study (which fit a 3.1 Å Fe-Fe distance) did not fit such a bridging atom.[38]

In this work, we took two complimentary approaches to testing the hypothesis that the active site of AlkB contains a bridged diiron center. We carried out x-ray absorption spectroscopy (XAS) and EXAFS studies on the diferric state of AlkB under non-reducing conditions. The Fe K-edge and pre-edge (which together comprise the x-ray absorption near edge structure, XANES) provide information of Fe site symmetry and relative oxidation state which complements the metrical information obtained from EXAFS.[48] We also carried out MD simulations informed by the EXAFS-confirmed metrics to determine whether potential conformational changes indicated that a protein-derived residue could come close enough to coordinate or bridge the iron ions.[49, 50]

EXPERIMENTAL METHODS:

PROTEIN EXPRESSION AND PURIFICATION:

DNA encoding *F. thermophila* AlkB (FtAlkB) (amino acids 4-399) was codon optimized and cloned into pET23 C-terminal His FLAG vector (provided by the Center for Membrane Protein Production and Analysis (COMPPA)). The protein was overexpressed in *E.coli* BL21(DE3). Cells were grown at 37 °C and induced with 0.2 mM IPTG. Cells were centrifuged 5 hours post-induction. Pelleted cells were resuspended in lysis buffer (20 mM HEPES pH 7.1, 150 mM NaCl with PSMF and DNase) and broken open with a French Press. FtAlkB was solubilized by 1% N-Dodecyl β-D-maltose (DDM)/0.1% cholesteryl hemisuccinate tris salt (CHS)

(Anatrace) and then isolated from the clarified supernatant and incubated with Ni NTA resin. Eluted protein was concentrated to a final concentration of ~1 mM as determined by a detergent-compatible Bradford assay (Pierce Thermo Scientific) as well as the measured absorbance of diluted samples at 280 nm using the calculated extinction coefficient (106925 M^{-1} cm^{-1}).

Variants were made using site-directed mutagenesis. Correct mutagenesis was confirmed using Sanger sequencing (Azenta). The miniprepped DNA was used to transform chemically competent BL21-DE3-star cells. These were plated on Luria-Bertani (LB)/agar plates with ampicillin. Primer information is provided in the SI (Text S1).

Measurement of enzymatic activity. Enzyme activity assays were conducted containing 800 μL clarified cell lysate from AlkB expressing cells, 200 μL clarified cell lysate from cells expressing an AlkB-specific rubredoxin AlkG and the corresponding rubredoxin-reductase AlkT[51-55], 100 μM ferrous ammonium sulfate (to ensure complete metalation of the protein)[56], 2 μL substrate, and 720 μM NADH. Alternatively, assays were done using 7 μM purified protein in buffer (20 mM Tris pH 7.4, 0.02% DDM, 150 mM NaCl), 100 μM ferrous ammonium sulfate, 7 μM purified rubredoxin, 2 μM purified maize ferredoxin reductase, 2 μL substrate, and 720 μM NADPH. Reactions were incubated at 37 °C while shaking at 250 rpm for 20 min. The reactions were quenched and extracted with 100 μL CH_2Cl_2 and vortexed for 40 s. The organic layer was removed and 1 μL injected onto an Agilent 7820A GC - 5977E Mass selective detector with an Agilent J&W HP-5 capillary column (30 m, 0.25 mm inner diameter, 0.5 μm film). The injector temperature was 225 °C, the initial oven temperature was 45 °C with a ramp of 10 °C per min to a final temperature of 220 °C.

XAS data collection: X-ray absorption data were collected at beamline I20 at Diamond Light Source under ring conditions of 300 mA at 3 GeV. The incident beam was monochromatized using a four-bounce Si(111) monochromator and harmonics were removed using Rh-coated and bare Si mirrors, the latter of which also focused the beam to ~1 x 1 mm at the sample. Energy calibration of the incident beam was achieved by setting the first inflection point of an Fe foil located downstream of the sample to 7112.0 eV. Samples were loaded into 2 mm thick aluminum or 3 mm thick polylactic acid (PLA) with polyetheretherketone (PEEK) slide-in slots sample holders which could accommodate multiple wells of sample and frozen in liquid nitrogen (schematic in Figure S1). During measurements, the samples were placed at 45° relative to the incident beam and maintained at <10 K using a liquid helium flow cryostat. A 64-element monolithic germanium detector (Canberra) was used to record the Fe Kα fluorescence.

Damage was assessed by collecting multiple, rapid X-ray absorption near edge structure (XANES) scans on the same spot of the sample until a change in the shape or position of the edge was observed. The AlkB samples were found to be highly sensitive to photoreduction and thus the incident beam was significantly attenuated (>99%) using 5.5 mm of graphite upstream of I0 and scans were constructed so as to minimize exposure time. To confirm sample stability, a quick edge scan was collected on the same spot after a full EXAFS scan, and the XANES were shown to overlay (Figure S2). Data were collected over the range of 7000 - 7700 eV and, as no fast shutter was present at the beamline, the total scan time, including data collection and motor moves, was kept to 600 s, conditions which allowed undamaged spectra to be obtained. Fresh spots were used for each scan. Samples were assayed for catalytic activity after irradiation and were found to retain activity (Figure S3).

Data analysis: For each scan, every channel of the 64-element detector was examined for evidence of ice diffraction or other spurious signals and was removed if such artefacts were found. All good detector channels from each scan were then averaged together and the averages examined for evidence of metallic Fe contamination, which can significantly impact the data analysis at the low Fe concentrations present in the samples; if found the scan was discarded. The resulting scans were imported to the Demeter suite of programs[57] and individually assessed for homogeneity to one another. All good scans were averaged in Athena, normalized to an edge jump of 1.0, and a background spline removed using an Rbkg factor of 1.1. Normalized XAS data were then exported and the XANES region fit using BlueprintXAS[58]; pre-edge areas are reported as the sum of pseudo-Voigt peak areas x100. EXAFS fitting was performed in k-space on k^3-weighted data in Artemis. Scattering paths were generated in FEFF from the reported cryo-EM structure[32] which had been manually modified to place the Fe centers at ~4 Å or ~3 Å from each other.

COMPUTATIONAL METHODS:

The recently determined cryo-EM structures of FtAlkB (PDB ID: 8SBB)[32] was used as the primary starting point for MD simulations, and the AlkB-AlkG natural fusion protein, FtAlkBG (PDB ID: 8F6T)[31] was also employed to estimate sensitivity to starting structure and sequence. The sequences of these two proteins are 50% identical and 64% similar, with all major active site residues conserved, as shown by performing a pairwise sequence alignment using the Needleman-Wunsch algorithm with the EMBOSS[59] server (Figure S4).

We embedded the AlkB protein in a phosphatidylethanolamine (POPE) lipid bilayer, which is a major constituent lipid of the *Ft* bacterial inner membrane in which the protein is found.[60] The LIPID21[61] forcefield, in combination with the ff14SB[62] forcefield for the protein and TIP3P[63] for water was chosen based on prior benchmarks against experiment on membrane properties.[64, 65] We employed the Orientation of Proteins in Membranes (OPM)[66] to estimate the position of AlkB in the membrane (Figure S5). CHARMM-GUI[67, 68] was used to construct the membrane around the aligned AlkB structure, and a pH of 7 was assumed for protonation states. The hydrogens added by CHARMM-GUI were compared with those predicted by the H++ server[69] to ensure consistency, and all assigned protonation states used for titratable residues are provided in the Supporting Information (Table S1). The replacement method was used to insert the protein into a POPE lipid bilayer with a 22.5 Å water layer modeled on the top or bottom of the membrane with a counterion concentration of 150 mM KCl salt. Additional details about the construction of the system are given in the Supporting Information (Text S2).

The force field parameters of each metal were built separately using the Metal Center Parameter Builder Python (MCPB.py)[70] tool used to assist with parameterization. Gaussian16[71] was employed to perform the density functional theory (DFT) calculations, which in this case corresponded to B3LYP[72-74] for the DFT exchange correlation functional. In each model, the iron was modeled as a high spin (S=5/2) Fe(III) center, and the LAN2LDZ effective core potential[75] used for the iron atom while the lighter elements were modeled using the 6-31G* basis set.[76-78] An additional set of parameters in which the iron centers were treated as high spin (S=4/2) Fe(II) was also fit. Derived charges and bonding force constants are available in the online Zenodo repository[79] where the naming scheme for parameterized residues is shown in the Supporting Information (Figure S6). A force field for the dodecane substrate was obtained using GAFF2[80] atom types, and charges were calculated with the AM1 semi-empirical Hamiltonian and fit using Antechamber.[81] Systems were equilibrated after a series of minimization steps, stepwise heating, and 200 ns NPT trajectories were propagated in triplicate for each system (Text S3). Weak harmonic restraints were applied to maintain the terminal carbon-Fe distance in the simulations and to maintain the average Fe-Fe distance to near the cryo-EM values (Figure S7, Text S3). DFT geometry optimizations performed on a small active site model including the two iron ions and all coordinating histidine sidechains with C_α atoms frozen to the cryo-EM structure position also showed an elongation of Fe-Fe distances (Text S4, Figure S8). GPU-accelerated pmemd in Amber22[82] was used to perform the production simulations, with additional simulation details and stepwise protocol given in the Supporting Information (Text S3). Cpptraj was used for analysis of all MD trajectories,[83] ChimeraX was used for structure visualization[84] and Jalview was used for sequence alignment visualization.[85] We propagated 3 x 200 ns production trajectories for various controls and studied experimental variants (Table S2) for a total of 8.4 μs.

RESULTS AND DISCUSSION:

Diiron proteins represent an important class of metalloproteins to which a diverse set of functions have been ascribed and[37, 86-89] the coordination chemistry of the two metal ions is generally central to their activity.[86-89] In this work, we resolve the apparent paradox presented by the observed distances between the two irons in both cryo-EM structures of AlkB (5.4-6.1 Å), and the previous observations of a short (3.1 Å) Fe-Fe vector in EXAFS.[38] We do so by revisiting the EXAFS characterization of the active site of AlkB and coupling that work to MD simulations. While EXAFS is unlikely to detect an Fe-Fe interaction at the 5.4 Å distance seen in the cryo-EM structure, it should detect a closely bonded single atom bridge (e.g. oxo / hydroxo at ~1.8 Å) and intermetallic scattering at the ≲ 4 Å distance seemingly required by the previous EXAFS and Mössbauer results.

To investigate the Fe environment in AlkB, we collected XAS and EXAFS data at several synchrotron facilities. Preliminary data collected at both the Cornell High Energy Synchrotron Source (CHESS) and Stanford Synchrotron Radiation Lightsource (SSRL) revealed that the ferric ions in AlkB are exquisitely sensitive to photoreduction, which severely limited the flux that could be applied to the sample. The restricted incident beam coupled to the inherent low concentration of the samples (~1 mM Fe) limited the data quality that could be obtained; these early data suggested the presence of scattering interactions beyond 3 Å (Figures S9 and S10), though in both cases the signal quality was insufficient to rigorously fit the data.

With the experience gained from our preliminary experiments, we were able to collect XANES and EXAFS data on undamaged AlkB with acceptable signal up to k = 12 from beamline I20 at Diamond Light Source. The pre-edge of wild-type AlkB was notably asymmetric and required two peaks to adequately fit the data (Figure 1, left); the intensity and intensity-weighted average energy (IWAE) of the pre-edge were consistent with ferric iron bound by light atoms in a low symmetry protein environment[48] (Table 1). Fits were also performed on the pre-edge from the E281A variant of AlkB (Figure 1, right). For this spectrum, the lower signal-to-noise led to only a single fit peak being required, though within experimental uncertainty the intensity and IWAE were both

identical to those from the wild-type enzyme. For both species, the pre-edge intensity was found to have a sizeable uncertainty—attributable to the close proximity of the rising edge—which allowed for variability in how the background was modeled.
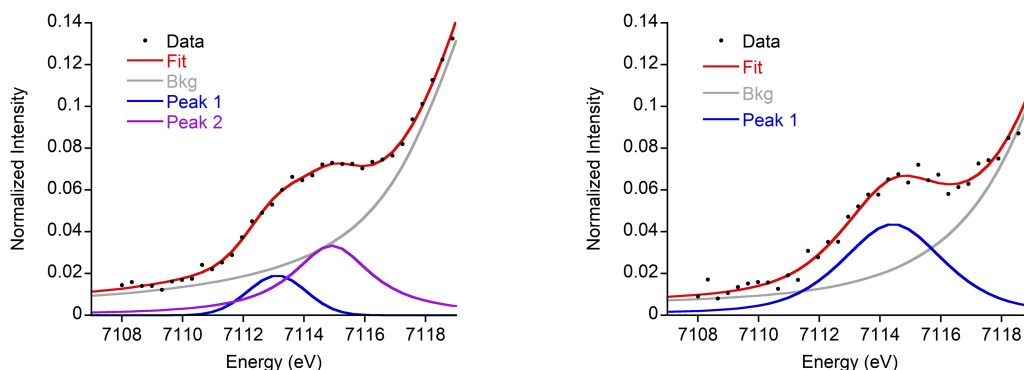

Figure 1: Fits to the pre-edges for wild-type (left) and E281A (right) AlkB samples are consistent with ferric ions in a low symmetry protein environment.

Table 1: Quantification of pre-edge fit parameters for wild-type and E281A AlkB

	Area[†]	IWAE	Num. Fits
Wild-type	21.3 ± 4.6 units	7114.3 ± 0.2 eV	71
E281A	24.4 ± 4.5 units	7114.5 ± 0.1 eV	65

[†] Areas are reported as the total integrated area of the pseudo-Voigt fit peaks x100.

The k^3-weighted EXAFS and corresponding Fourier transform (FT) of the data on wild-type AlkB from k = 2 – 11.5 are shown in Figure 2. The FT data have not been phase-corrected, and so the apparent distances revealed by reading directly off the FT (R+Δ) are systematically shorter by 0.3 – 0.5 Å relative to the true distances; this offset is accounted for in the fit data presented in Table 2. For the sake of discussion, distance values read from the FTs are explicitly reported as R+Δ values while those obtained from fitting (the true interatomic distances) are reported without this qualifier. The EXAFS reveal an intense first shell of scatterers at R+Δ ≈ 1.6 Å as well as the presence of multiple shells of longer range scattering out to R+Δ values of nearly 4 Å. The FT shows no clear evidence for a bridging Fe-oxo bond, which should appear at R+Δ ≈ 1.3 – 1.4 Å and thus be resolved from the main first shell scattering given the experimental resolution of ~0.17 Å.
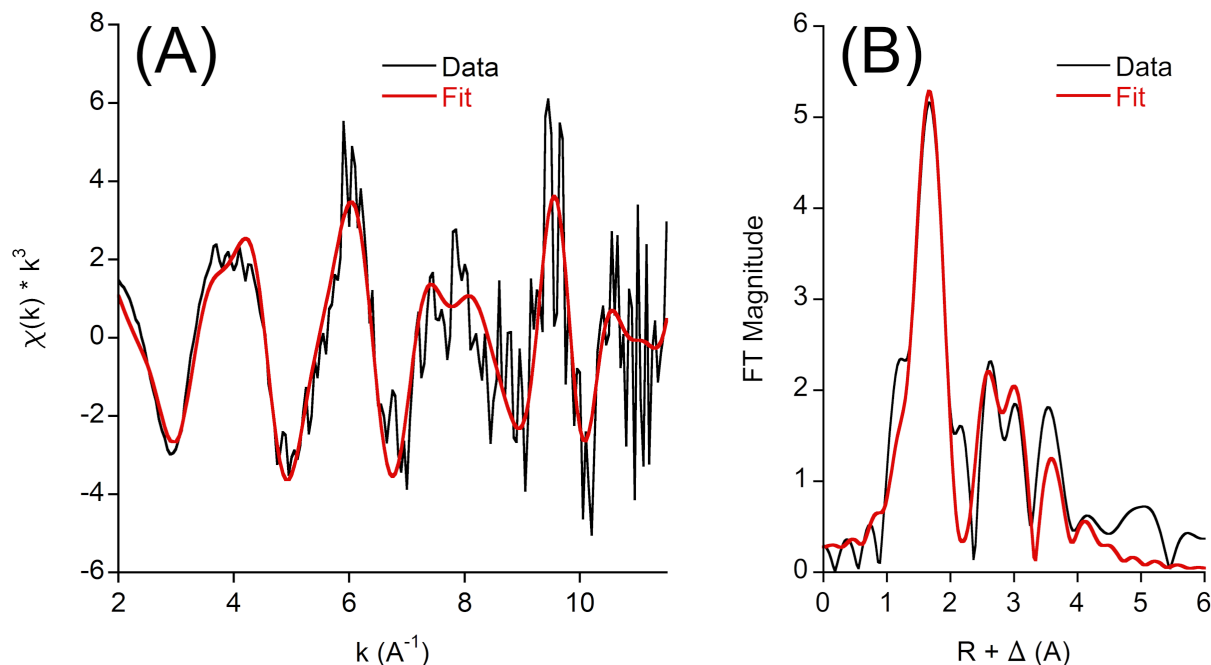
Figure 2: EXAFS data with k^3-weighting together with the best fit (fit 8) are shown in panel A and the corresponding Fourier transforms of the data and fit from k = 2.0 – 11.5 are shown in panel B.

These data immediately prompt the question of whether the long distance (R > 3 Å) scattering originates from a nearby Fe ion or from light atoms. Light atom scattering often has negligible FT intensity at such extended distances, though rigid planar ligands can gain significant long-range intensity due to the presence of multiple scattering; indeed, previous work on metal-imidazole complexes has revealed both the presence of long-range light atom scattering at distances >3 Å and also the necessity of including multiple scattering in order to obtain correct fits.[46, 90, 91] Thus, the present case of AlkB, with its homoleptic histidine first coordination shell, presents the need to carefully interrogate whether the long-range scattering observed in the data results from light atoms or from a nearby metal ion.

To resolve this question, fits to the data were performed with a variety of combinations of light and metallic scattering partners; the results from over 500 individual fits are available in our Zenodo repository[79] and the best of those fits are summarized in Table 2. In brief, fits 1 – 3 rely solely on single scattering while fits 4 – 8 incorporate single and multiple scattering paths; fits 1, 4, 5, and 8 made use of only light atom scattering paths while fits 2, 3, 6, and 7 incorporated an Fe scatterer.

Regardless of the specific paths included in the fit, the first shell Fe-N distance was always found at 2.12 – 2.15 Å while a second sphere Fe-C was observed at 3.14 – 3.15 Å. These distances are consistent with previous crystallographic characterization of high spin ferric-imidazole systems.[92-96] For modeling the interactions observed at longer distances, when only single scattering was considered—fits 1 – 3—acceptable fits could be obtained with either light or metallic scattering partners (Table 2). Inclusion of an Fe at either ~3.1 or ~4.1 Å resulted in statistically improved fits relative to the light-atom-only fit 1, with the best overall fit among this group having a partial occupancy (coordination number = 0.6) Fe scatterer at 4.09 Å; the corresponding fit with Fe-N scattering at 4.40 Å possessed a decidedly inferior R-factor. Thus, for an analysis that does not account for multiple scattering, it would be reasonable to conclude that AlkB possesses an Fe-Fe separation of 4.09 Å or even 3.12 Å.

Visual inspection of the FTs for fits 1 – 3 revealed areas of notable disagreement with the experimental data around R+Δ values of 2.6 and 3.6 Å (Figure S11), suggesting that this fitting approach systematically failed to account for a portion of the scattering. Following the methodology of previous groups who have fit imidazole-coordinated metal centers, we incorporated multiple scattering paths into our fits in an attempt to better fit these regions of the data.[90, 91, 93, 94, 96] For fits 4 and 5, we maintained the number of fit components at three by replacing the long-distance N/Fe scatterer from fits 1 – 3 with light atom multiple scattering: Fe-N-C scattering at ~3.3 Å in fit 4 and Fe-N-N scattering at ~4.3 Å in fit 5. Both fits 4 and 5 improved on the quality of the light-atom-only fit 1 and, notably, the inclusion of multiple scattering at 3.29 Å resulted in a statistically identical

quality fit as the Fe-containing fit 2. Taken together, the results from the three component fits show that an Fe scatterer *cannot be unambiguously demonstrated* in the data from AlkB.

Furthermore, since all of the three component fits fail to fully reproduce the FT over its full range of R+Δ = 1 – 4 Å, the number of components was increased to five in an attempt to fit the entire distance range (fits 7 and 8). Both of these fits perform much better at reproducing the full FT and both capture all of the main interactions. Based solely on the statistics, fit 7, with an Fe-Fe vector at 4.11 Å, is marginally superior to the light-atom-only fit 8. Closer investigation, however, reveals that fit 7 places nitrogen scatterers at a distance of 4.69 Å from the Fe center. A simple, static model of an idealized Fe-histidine interaction with an Fe-N bond length of 2.14 Å (Figure S12) demonstrates that this distance is much too long to be compatible with the distal N/C atoms of the imidazole ring. Fit 8, on the other hand, places this longer-range Fe-N interaction at 4.40 Å, which is much more consistent with the simple model (Figure S12).

Table 2: Parameters for N, R, and σ^2 employed in the best fits to the EXAFS data[†]

		Fit 1	Fit 2	Fit 3	Fit 4	Fit 5	Fit 6	Fit 7	**Fit 8**
# Components		3	3	3	3	3	4	5	**5**
Fe-N	N	4	4	4	4	4	4	4	**4**
(single)	R	2.13	2.13	2.12	2.15	2.13	2.14	2.15	**2.14**
	σ^2	6.41	6.58	6.53	6.30	6.44	6.45	6.46	**6.30**
Fe-C	N	4.5	4.5	---	5.5	4.5	5.5	6	**5.5**
(single)	R	3.14	3.14	---	3.15	3.14	3.15	3.15	**3.14**
	σ^2	1.50	1.47	---	1.44	1.57	1.29	1.74	**1.08**
Fe-N-C	N	---	---	---	11.5	---	11	12	**12**
(multiple)	R	---	---	---	3.29	---	3.29	3.29	**3.29**
	σ^2	---	---	---	1.58	---	1.31	1.25	**1.03**
Fe-N	N	3	---	3.5	---	---	---	6	**7**
(single)	R	4.40	---	4.39	---	---	---	4.69	**4.40**
	σ^2	1.99	---	2.08	---	---	---	9.57	**1.09**
Fe-Fe	N	---	0.6	0.7	---	---	0.6	0.9	**---**
(single)	R	---	4.09	3.12	---	---	4.10	4.11	**---**
	σ^2	---	1.18	1.30	---	---	1.18	3.33	**---**
Fe-N-N	N	---	---	---	---	5	---	---	**13**
(multiple)	R	---	---	---	---	4.33	---	---	**4.51**
	σ^2	---	---	---	---	1.64	---	---	**5.66**
E_0		2.14	2.55	0.20	4.51	1.90	4.26	4.65	**3.19**
R-factor		0.370	0.352	0.361	0.352	0.360	0.326	0.315	**0.322**

[†] All distances are in Å, E_0 values are in eV, and σ^2 values are reported as x10^3. The S_0^2 value was fixed at 1.0 for all fits.
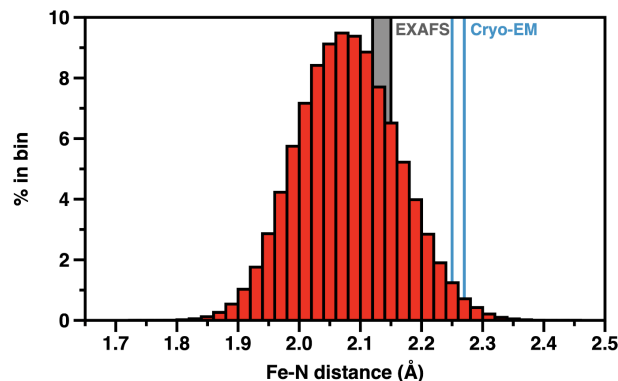
Figure 3: Histogram of Fe-N distances observed in wild-type holo *Ft*AlkB Fe(III)/Fe(III) MD simulations. The range observed in the EXAFS fits are denoted by a gray shaded region from 2.12 - 2.15 Å and the two distances observed in the cryo-EM structures, 8SBB and 8F6T, are given as two blue bars at 2.25 Å and 2.27 Å, respectively. The bin size for the simulation data given in red is 0.02 Å.

In summary, the EXAFS data on AlkB are best fit with Fe-histidine light atom scattering and do not require an Fe-Fe scattering vector at closer than 4 Å, results that are fully consistent with the recent cryo-EM structures. The lack of apparent Fe scattering at the cryo-EM distance of 5 – 6 Å is unsurprising given that EXAFS intensity decays exponentially as distance increases. The analysis here stands in contrast to that presented by Tsai in 2017[38], where an Fe-Fe interaction was fit at ~3.1 Å. The conclusion of that study can be rationalized given that their fitting procedure did not employ multiple scattering to model the longer-range interactions, which was found to be essential in our analysis.

MOLECULAR DYNAMICS

To allow interrogation of conformational motions and key hydrogen bonding networks in FtAlkB, we first ensured that our models were representative of experiment. Accurate representation of the metal center geometry is crucial, so we compared our parameters fit from DFT calculations (see Computational Details) to the EXAFS-derived distances. The average equilibrium Fe(III)—N distance of 2.08 Å and Fe(II)—N distance of 2.14 Å arising directly from the parameterization compare well to the distance from the best EXAFS fits which are ~2.14 Å (Table 2, Table S3). The Fe(II) parameters agree well with the EXAFS data, indicating that there is slight systematic underestimation in the bond lengths likely attributed to the functional or basis set employed in the DFT optimizations as the protein has a confirmed ferric oxidation state. As expected, the average distances sampled by our MD simulations are near the parameterized equilibrium values, with standard deviations of ~0.07 Å, indicating MD simulations sample geometries similar to the DFT optimized structure (Table S3). Nevertheless, these distances are more consistent with the EXAFS data than with the 2.25-2.27 Å bond lengths observed in cryo-EM structures (Figure 3, Table S3, Figure S13). The distances from the iron center to the distal nitrogen and carbon in the histidine ring are also consistent with EXAFS measurements. While the distances sampled by MD are slightly shorter due to the underestimation of the Fe-N bond length, after shifting the first shell Fe-N distance by only ~0.06 Å, these longer-range distances would be in excellent agreement with the experimentally-determined data (Figure S12, Table S4). The metal center geometry across simulations compared to the starting cryo-EM structure geometry retains an average Cα RMSD of 0.85 Å (Figure S14) and overlays well.

The stability of the protein in our MD simulations is quite similar across all sets of simulations, where the average root-mean square deviation of the backbone Cα positions with respect to the cryo-EM structure hovers around 1.4 – 2.0 Å (Figures S15 – S18). The larger values in this range are attributed to simulations we propagated without the metal center or substrate, which is seen across FtAlkB and FtAlkBG simulations (Figures S15, S17-S18). This is rationalized by examining the root-mean square fluctuations of the sidechains, with more flexible loop regions having higher RMSFs while the transmembrane helices are the most rigid as expected (Figures S19-S22). The main difference between these simulations in terms of global stability is seen when comparing the apo to holoenzyme simulations, where residues that coordinate the iron are much more flexible when the metal is removed, and these changes in flexibility impact nearby residues propagating through the protein (Figure S23).

To determine if key carboxylates E281 and D190 could play a role as a bridging ligand or in catalysis, we examined their relative locations and hydrogen bonding partners. E281 is the obvious candidate for a bridging ligand or catalytic role based on its positioning in the cryo-EM structure and adjacency to the terminal carbon in the active site. However, we do not see evidence that this residue comes close enough to coordinate the 4His coordinated-metal frequently, let alone bridge the two irons in our simulations. By examining the closest carboxylate atom to each iron center over time the closest distance sampled for FtAlkB Fe(III) simulations are ~6.0 Å from E281 to the 5His coordinated- metal in the production simulation, and the distance to the more natural coordination partner, Fe4His, is only below 3 Å a small fraction of the time (Figure S24). When comparing our simulations with the di-iron center with the ferrous parameters, these distances are even longer due to decreased electrostatic attraction. In the FtAlkBG structure, the residue that corresponds to E281 (E271) explicitly coordinates the Fe4His iron center, but we did not parameterize this form or enforce this coordination as to allow free movement of the residue. While our classical MD simulations have fixed charges and cannot be sampled on the timescale where whole-domain motions would be expected, we would expect that the attractive electrostatic interaction should lead to a decrease in these distances. It is possible that a bridging ligand could form with a longer Fe-Fe distance or if the substrate was not present, due to decreased steric hindrance to rearrangement. However, we do not see the distance between the closest carboxylate atom of E281 and the Fe5His markedly decrease in this case either (Figure S24). Recently, a computational study examined the mechanism of oxidation by alkanes in AlkB, but did not examine possible active site structures with protein derived bridging ligands. While this study included the protein environment in a MD followed by QM/MM approach, the authors did not analyze conformational fluctuations, and are unable to do so as the metal center was frozen during MD sampling.[97]
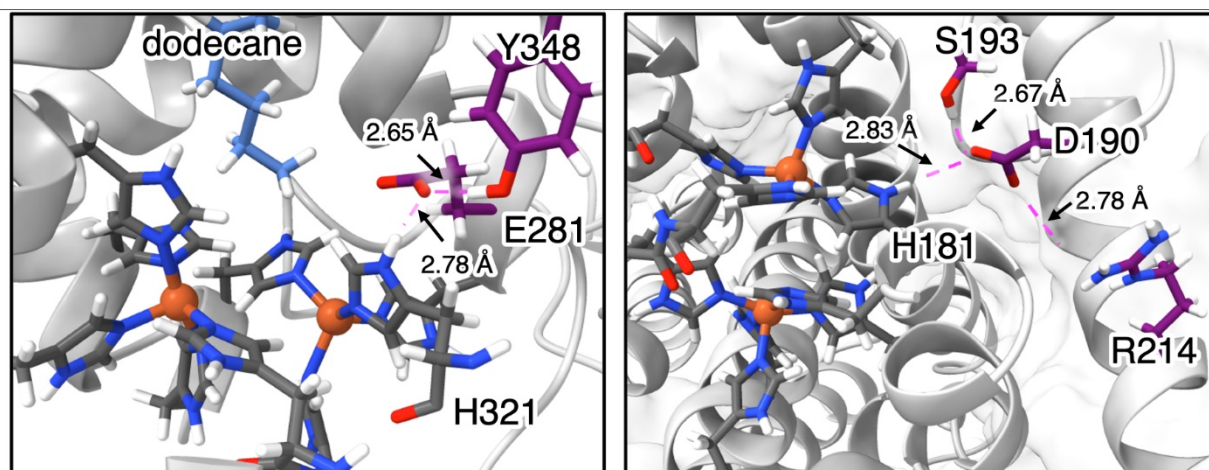

Figure 4. Key residues involved in protein-protein hydrogen bonds involving E281 (left) or D190 (right). The metal center is rotated and the dodecane substrate is omitted for ease of visualization on the right-hand side. Dashed pink lines denote the hydrogen bonding interactions observed with labels given corresponding to the average distance observed in the *Ft*AlkB holo wild-type trajectories. The representative frames chosen for visualization may not have the exact distances that correspond to the labeled averages.

To further examine if E281 was playing a key role in stabilizing the active site geometry, we scrutinized the hydrogen bonds. One prevalent hydrogen bond is apparent through all of the simulations, which is Y348 donating a hydrogen bond to the E281 carboxylate (Figure 4). In addition to prevalence of >97% in wild-type holo simulations, it has a short donor-acceptor heavy atom distance, with an average and minimum distance of 2.65 Å and 2.38 Å, respectively (Figure S25, Table S5). The distance observed is characteristic of a short strong hydrogen bond, such as are typically observed between glutamate/aspartate and tyrosine or serine.[98] It is debated if these shortened distances are invoked in enzyme catalysis due to a presumably lower energy barrier to proton transfer,[99] but given the activity of E281A, this residue would not be suspected to play a vital role in catalysis.[32] E281 can also hydrogen bond with water, or the distal nitrogen hydrogen of metal center coordinating residue H321 (Table S5). The interaction with water is on average >30% of the FtAlkB trajectories, with high variability across systems studied (Table S). If the substrate or metals are absent, this frequency increases as expected due to the increased flexibility of these residues in the apo form and lack of the hydrophobic substrate in the binding site. Regardless, of the individual variation in frequency of hydrogen bond

occurrence, this analysis shows that multiple hydrogen bonds can be formed at once, with one or both carboxylate oxygen interacting with multiple hydrogen bond donors.

To investigate the potential impacts of perturbing the E281 hydrogen bonding network, we studied the variants Y348F, E281A, and E281L, which abolishes the ability to form this hydrogen bond. However, we see no change in overall protein stability on the timescale of this work (Figure S16,S20). The Y348F variant shows a smaller percentage of hydrogen bonding between E281 and H321 or water than wild-type, but no other indications of conformational changes (Table S5, Figure S26). We also simulated the E281K variant, and with the assumption that the protein still adopts the same primary fold, we see that there is a new hydrogen bond between the K281 sidechain NH_3^+ and Y348 hydroxyl 10% of the time. However, the sidechain instead faces away from the active site, forming new hydrogen bonds with other polar residues (Table S5, Figure S26). Given the large size of lysine and the positive charge next to the metal center, it is reasonable to expect this rearrangement.

We examined our simulation data to attempt to ascribe the role of the D190 carboxylate. D190 is too far to coordinate either metal, remaining at distances greater than 6 or 9 Å, from the 4-coordinate His or the 5-coordinate His, respectively (Figure S27). These distances are well maintained from the cryo-EM structure suggesting no rearrangement. Hydrogen bonds are observed between the D190 carboxylate and the side chains of S193, R214, H181 (Figure 4, Table S6). The hydrogen bonding interaction between S193 and D190 is slightly less prevalent than E281-Y348 (87 %), but still characteristic of a short hydrogen bond and similarly observed across systems studied (Table S6). The only hydrogen bond that could be hypothesized to play a clear functional role is the hydrogen bond between D190 and H181, reminiscent of the hydrogen bond noted in PEDS1.[42] While this interaction is a minor population of the total hydrogen bonds we observe, this interaction may contribute to active site stability, as H181 coordinates the undercoordinated Fe (Table S6). These hydrogen bonds are not surprising given the residues location in the cryo-EM structure, where these resides are all near the D190 sidechain, suggesting no major rearrangements from the FtAlkB cryo-EM structure.[32]

BIOCHEMICAL CHARACTERIZATION

Structural variants of the residues D190 and E281 were prepared to further interrogate the hypothesis that the iron ions are bridged by a carboxylate-containing residue. PpD181A (PpD181 is analogous to FtD190) had previously been shown to be inactive, leading to the suggestion that D181 could provide the putative carboxylate bridge seen in many other diiron enzymes.[17] As described above, however, in both cryo-EM structures, this residue is too far from either iron ion to even be considered a ligand, much less the source of a covalent bridge between the two iron ions (Figure S27, Table S6) and never appears close enough in the MD simulations to ligate or bridge. The residue is only partially conserved among the class-III diiron proteins, whose active sites are thought to be identical.[17] Nevertheless, the activity of FtD190A was substantially reduced relative to the wild-type, showing approximately 10% of wild-type activity when queried over the range of standard FtAlkB substrates (Figure 5). Mutating glutamate to an aspartate (D190E) led to a variant with even lower activity. Thus, while cryo-EM, EXAFS, MD data, and sequence alignment all suggest that D190 does not provide a carboxylate bridge between the two iron ions, functional data suggests it is important for the activity of AlkB.

Cryo-EM structures of AlkB suggest that E281 is a much better candidate to be a bridging ligand. We have previously demonstrated that E281A is active.[32] In this work, we prepared two additional variants, E281L and E281K. E281K is as active as the wild-type, while E281L is less active (Figure 5). These results are also inconsistent with the hypothesis that E281 provides ligands to the two iron ions or that the protein is sensitive to the charge or size of the residue at this position. MD simulations pointed to strong H-bonding interaction between E281 and Y348, which was diminished only for simulations conducted in the apo form, without iron bound (Table S5). We made a variant, Y348F, to probe the functional significance of this interaction. The Y348F was slightly diminished in activity relative to the wild-type, but overall no significant effect was attributable to this structural change (Figure 5).
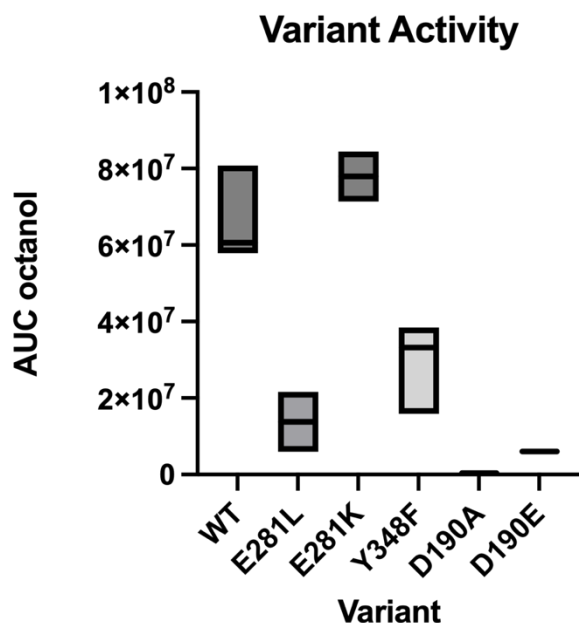
Variant Activity

Figure 5. Relative activity of wild-type and amino acid variants quantified by oxidation of octane as measure by the area under the octanol peak detected by GC-MS. The horizontal line represents the average value from the individual measurements and the top and bottom of the boxes represent the maximum and minimum values obtained from at least two biological replicates.

CONCLUSION

In summary, the EXAFS analysis presented herein is consistent with the published cryo-EM structures studies and demonstrates that the data is most rigorously fit with only light atom scattering resulting from the coordinating histidine residues. MD simulations were consistent with the EXAFS analysis and show no evidence of a protein derived bridging ligand arising from nearby carboxylate residues, E281 and D190. Biochemical experiments show that the active site glutamate residue, E281, is not essential for activity. In fact, mutating it to a lysine retains a high level of activity. Further corroborating this, the XANES spectrum of the E281A variant is indistinguishable from the wild-type within experimental uncertainty. D190 plays an important, but currently unassigned, functional role, perhaps altering the electronic structure of a ligating histidine through hydrogen bonding. In sum, these data underscore the unusual nature of the diiron active site of AlkB, and the class-III diiron proteins more generally, and make more urgent the need to understand the distribution of electrons and protons in the catalytic reaction cycle.

Corresponding Authors

*email: rna2113@columbia.edu, cjp227@cornell.edu

Present Addresses

†Juliet A. Lee, Department of Chemistry and Chemical Engineering, California Institute of Technology, Pasadena CA 91125 USA

Lauren Hendricks, Midwestern University Chicago College of Osteopathic Medicine, Downers Grove, IL 60515 USA, Tierani Green, Massachusetts Institute of Technology, Cambridge, MA 02139, USA

Author Contributions

The manuscript was written through contributions of all authors. / All authors have given approval to the final version of the manuscript. /

Notes

The authors declare no competing interests.

Supporting Information.

   Additional details for molecular dynamics simulation setup and equilibration, additional EXAFS for fits 1 – 7, and primer sequences (PDF).

This material is available free of charge via the Internet at http://pubs.acs.org.

ABBREVIATIONS AlkB, alkane monooxygenase; EXAFS, Extended X-ray Absorption Fine Structure; MD, molecular dynamics; GC-MS gas chromatography-mass spectrometry; IPTG Isopropyl β- d-1-thiogalactopyranoside, XAS, x-ray absorption spectroscopy

REFERENCES

   (1) Belhaj, A.; Desnoues, N.; Elmerich, C. Alkane biodegradation in Pseudomonas aeruginosa strains isolated from a polluted zone: identification of alkB and alkB-related genes. *Res. Microbiol.* **2002**, *153* (6), 339-344, DOI: https://doi.org/10.1016/S0923-2508(02)01333-5
   (2) Heiss-Blanquet, S.; Benoit, Y.; Maréchaux, C.; Monot, F. Assessing the role of alkane hydroxylase genotypes in environmental samples by competitive PCR. *J. Appl. Microbiol.* **2005**, *99* (6), 1392-1403, DOI: 10.1111/j.1365-2672.2005.02715.x
   (3) Karthikeyan, S.; Hatt, J. K.; Kim, M.; Spain, J. C.; Huettel, M.; Kostka, J. E.; Konstantinidis, K. T. A novel, divergent alkane monooxygenase (alkB) clade involved in crude oil biodegradation. *Environ. Microbio. Reports* **2021**, *13* (6), 830-840, DOI: https://doi.org/10.1111/1758-2229.13018
   (4) Long, H.; Wang, Y.; Chang, S.; Liu, G.; Chen, T.; Huo, G.; Zhang, W.; Wu, X.; Tai, X.; Sun, L.; et al. Diversity of crude oil-degrading bacteria and alkane hydroxylase (alkB) genes from the Qinghai-Tibet Plateau. *Environ. Monit. Assess.* **2017**, *189* (3), 116, DOI: 10.1007/s10661-017-5798-5
   (5) Nie, Y.; Chi, C.-Q.; Fang, H.; Liang, J.-L.; Lu, S.-L.; Lai, G.-L.; Tang, Y.-Q.; Wu, X.-L. Diverse alkane hydroxylase genes in microorganisms and environments. *Sci. Rep* **2014**, *4* (1), 4968, DOI: 10.1038/srep04968
   (6) Throne-Holst, M. M., S.; Winnberg, A.; Ellingsen T. E; Kotlar, E.-K.; Zotchev, S. B. Utilization of *n*-alkanes by a newly isolated strain of *Acinetobactervenetianus*: the role of two AlkB-type alkane hydroxylases. *Appl. Microbiol. Cell Phys.* **2006**, *72*, 353-360,

(7) Van Beilen, J. B.; Marín, M. M.; Smits, T. H. M.; Röthlisberger, M.; Franchini, A. G.; Witholt, B.; Rojo, F. Characterization of two alkane hydroxylase genes from the marine hydrocarbonoclastic bacterium Alcanivorax borkumensis. *Environ. Microbio* **2004**, *6* (3), 264-273, DOI: https://doi.org/10.1111/j.1462-2920.2004.00567.x

(8) van Beilen, J. B.; Panke, S.; Lucchini, S.; Franchini, A. G.; Röthlisberger, M.; Witholt, B. Analysis of Pseudomonas putida alkane-degradation gene clusters and flanking insertion sequences: evolution and regulation of the alk geness. *Microbiol* **2001**, *147* (6), 1621-1630, DOI: https://doi.org/10.1099/00221287-147-6-1621

(9) Vomberg, A.; Klinner, U. Distribution of alkB genes within n-alkane-degrading bacteria. *J. Appl. Microbiol.* **2000**, *89*, 339-348,

(10) Wang, L.; Wang, W.; Lai, Q.; Shao, A. Gene diversity of CYP153A and AlkB alkane hydroxylases in oil-degrading bacteria isolated from the Atlantic Ocean. *Environ. Microbiol.* **2010**, *12*, 1230-1242,

(11) Wang, W.; Wang, L.; Shao, Z. Diversity and Abundance of Oil-Degrading Bacteria and Alkane Hydroxylase (*alkB*) Genes in the Subtropical Seawater of Xiamen Island. *Microb. Ecol.* **2010**, *60*, 429-439,

(12) Wang, Y.; Nie, M.; Wan, Y.; Tian, X.; Nie, H.; Zi, J.; Ma, X. Functional characterization of two alkane hydroxylases in a versatile Pseudomonas aeruginosa strain NY3. *Ann. Microbiol.* **2017**, *67* (7), 459-468, DOI: 10.1007/s13213-017-1271-5

(13) Wasmund, K.; Burns, K. A.; Kurtboke, D. I.; Bourne, D. G. Novel Alkane Hydroxylase Gene (*alkB*) Diversity in Sediments Associated with Hydrocarbon Seeps in the Timor Sea, Australia. *Appl. Environ. Microbiol.* **2009**, *75* (23), 7391-7398,

(14) Zhou, Z.; Qiang, L.; Hao, C.; Fang-ming, L.; Yi-bin, W.; Ning, D.; Jin-lai, M. Molecular Cloning and Characterization of the alkB gene of Shewanella sp. NJ49 from Antarctic Sea Ice. *J. Pure Appl. Microbiol.* **2014**, *8*, 3429-3438,

(15) McKenna, E. J.; Coon, M. J. Enzymatic ω-Oxidation: IV Purification and Properties of the ω-Hydroxylase of Pseudomonas oleovorans. *J. Biol. Chem.* **1970**, *225*, 3882-3890,

(16) Shanklin, J.; Achim, C.; Schmidt, H.; Fox, B. G.; Münck, E. Mossbauer studies of alkane omega-hydroxylase: Evidence for a diiron cluster in an integral-membrane enzyme. *Proc. Natl. Acad. Sci.* **1997**, *94*, 2981-2986, DOI: 10.1073/pnas.94.7.2981

(17) Shanklin, J.; Whittle, E. Evidence linking the Pseudomonas oleovorans alkane omega-hydroxylase, an integral membrane diiron enzyme, and the fatty acid desaturase family. *FEBS Lett.* **2003**, *545*, 188-192, DOI: 10.1016/s0014-5793(03)00529-5

(18) Iqbal, T.; Murugan, S.; Rajendran, K.; Sidhu, J. S.; Das, D. Unraveling the Conversion of Fatty Acids into Terminal Alkenes by an Integral Membrane Enzyme, UndB. *ACS Catal.* **2023**, 15516-15525, DOI: 10.1021/acscatal.3c04171

(19) Bard, M.; Bruner, D. A.; Pierson, C. A.; Lees, N. D.; Biermann, B.; Frye, L.; Koegel, C.; Barbuch, R. Cloning and characterization of ERG25, the Saccharomyces cerevisiae gene encoding C-4 sterol methyl oxidase. *Proc. Acad. Nat. Sci.* **1996**, *93*, 186-190,

(20) Kim, S. H.; Steere, L.; Zhang, Y.-K.; McGregor, C.; Hahne, C.; Zhou, Y.; Liu, C.; Cai, Y.; Zhou, H.; Chen, X.; et al. Inhibiting C-4 Methyl Sterol Oxidase with Novel Diazaborines to Target Fungal Plant Pathogens. *ACS Chem. Biol.* **2022**, *17* (6), 1343-1350, DOI: 10.1021/acschembio.2c00257

(21) Ye, R. W.; Stead, K. J.; Yao, H.; He, H. Mutational and functional analysis of the beta-carotene ketolase involved in the production of canthaxanthin and astaxanthin. *Appl. Environ. Microbiol.* **2006**, *72* (9), 5829-5837, DOI: 10.1128/aem.00918-06

(22) Wu, S.; Zhou, Y.; Gerngross, D.; Jeschek, M.; Ward, T. R. Chemo-enzymatic cascades to produce cycloalkenes from bio-based resources. *Nat. Commun.* **2019**, *10* (1), 5060, DOI: 10.1038/s41467-019-13071-y

(23) Rui, Z.; Harris, N. C.; Zhu, X.; Huang, W.; Zhang, W. Discovery of a Family of Desaturase-Like Enzymes for 1-Alkene Biosynthesis. *ACS Catal.* **2015**, *5* (12), 7091-7094, DOI: 10.1021/acscatal.5b01842

(24) van Beilen, J. B.; Kingma, J.; Witholt, B. Substrate specificity of the alkane hydroxylase system of *Pseudomonas oleovorans* GPo1. *Enzyme Microb. Technol.* **1994**, *16*, 904-911,

(25) May, S. W.; Abbott, B. J. Mechanistic Studies on Non-Heme Iron Monooxygenase Systems of *Pseudomonas oleovorans*. *Biochem. Biophys. Res. Commun.* **1972**, *48*, 1230-1234,

(26) May, S. W.; Gordon, S. L.; Steltenkamp, M. S. Enzymatic epoxidation of trans,trans-1,8-dideuterio-1,7-octadiene. Analysis using partially relaxed proton Fourier transform NMR. *J. Am. Chem. Soc.* **1977**, *99* (7), 2017-2024, DOI: 10.1021/ja00449a001

(27) May, S. W.; Katopodis, A. G. Oxygenation of alcohol and sulphide substrates by a prototypical non-haem iron monooxygenase: catalysis and biotechnological potential. *Enzyme Microb. Technol.* **1986**, *8* (1), 17-21, DOI: https://doi.org/10.1016/0141-0229(86)90004-9

(28) May, S. W.; Schwartz, R. D. Stereoselective epoxidation of octadiene catalyzed by an enzyme system of Pseudomonas oleovorans. *J. Am. Chem. Soc.* **1974**, *96* (12), 4031-4032, DOI: 10.1021/ja00818a060

(29) May, S. W.; Steltenkamp, M. S.; Schwartz, R. D.; McCoy, C. J. Stereoselective Formation of Diepoxides by an Enzyme System of Pseudomonas oleovorans. *J. Am. Chem. Soc.* **1976**, *98*, 7856-7858,

(30) Naing, S.-H.; Parvez, S.; Pender-Cudlip, M.; Groves, J. T.; Austin, R. N. Substrate specificity and reaction mechanism of purified alkane hydroxylase (AlkB) from the hydrocarbonoclastus bacterium Alcanivorax borkumensis. *J. Inorg. Biochem.* **2013**, *121*, 46-52,

(31) Chai, J.; Guo, G.; McSweeney, S. M.; Shanklin, J.; Liu, Q. Structural basis for enzymatic terminal C–H bond functionalization of alkanes. *Nat. Struct. Mol. Biol.* **2023**, *30* (4), 521-526, DOI: 10.1038/s41594-023-00958-0

(32) Guo, X.; Zhang, J.; Han, L.; Lee, J.; Williams, S. C.; Forsberg, A.; Xu, Y.; Austin, R. N.; Feng, L. Structure and mechanism of the alkane-oxidizing enzyme AlkB. *Nat. Commun.* **2023**, *14* (1), 2180, DOI: 10.1038/s41467-023-37869-z

(33) Wang, H.; Klein, M. G.; Zou, H.; Lane, W.; Snell, G.; Levin, I.; Li, K.; Sang, B.-C. Crystal structure of human stearoyl-coenzyme A desaturase in complex with substrate. *Nat. Struct. Mol. Biol.* **2015**, *22* (7), 581-585, DOI: 10.1038/nsmb.3049
http://www.nature.com/nsmb/journal/v22/n7/abs/nsmb.3049.html#supplementary-information

(34) Bai, Y.; McCoy, J. G.; Levin, E. J.; Sobrado, P.; Rajashankar, K. R.; Fox, B. G.; Zhou, M. X-ray structure of a mammalian stearoyl-CoA desaturase. *Nature* **2015**, *524* (7564), 252-256, DOI: 10.1038/nature14549

(35) Zhu, G.; Koszelak-Rosenblum, M.; Connelly, S. M.; Dumont, M. E.; Malkowski, M. G. The Crystal Structure of an Integral Membrane Fatty Acid alpha hydroxylase. *J. Biol. Chem.* **2015**, *290*, 29820-29833, DOI: 10.1017/jbc.M115.680124

(36) Shen, J.; Wu, G.; Tsai, A.-L.; Zhou, M. Structure and mechanism of a unique diiron center in mammalian stearoyl-CoA desaturase. *J. Mol. Biol.* **2020**, *432*, 5152-5161,

(37) Lippard, S. J. Hydroxylation of C-H bonds at carboxylate-bridge diiron centres. *Philos. Trans. R. Soc. London, Ser. A* **2005**, *363*, 861-877,

(38) Tsai, Y.-F.; Luo, W.-I.; Chang, J.-L.; Chang, C.-W.; Chuang, H.-C.; Ramua, R.; Wei, G.-T.; Zen, J.-M.; Yu, S. S.-F. Electrochemical Hydroxylation of C3-C12 n-Alkanes by Recombinant Alkane Hydroxylase (AlkB) and Rubredoxin-2 (AlkG) from Pseudomonas putida GPo1. *Sci. Rep* **2017**, *7*, 8369, DOI: DOI:10.1038/s41598-017-08610-w

(39) Roongta, U. V.; Pabalan, J. G.; Wang, X.; Ryseck, R.-P.; Fargnoli, J.; Henley, B. J.; Yang, W.-P.; Zhu, J.; Madireddi, M. T.; Lawrence, R. M.; et al. Cancer Cell Dependence on Unsaturated Fatty Acids Implicates Stearoyl-CoA Desaturase as a Target for Cancer Therapy. *Mol. Cancer Res.* **2011**, *9* (11), 1551, DOI: 10.1158/1541-7786.MCR-11-0126

(40) Groves, J. T.; Feng, L.; Austin, R. N. The structure and function of alkane monooxygenase (AlkB). *Acc. Chem. Res.* **2023**, *56* (24), 3665–3675,

(41) Strange, R. W.; Feiters, M. C. Biological X-ray absorption spectroscopy (BioXAS): a valuable tool for the study of trace elements in the life sciences. *Curr. Opin. in Struct. Biol.* **2008**, *18* (5), 609-616, DOI: https://doi.org/10.1016/j.sbi.2008.06.002

(42) Werner, E. R.; Fernández-Quintero, M. L.; Hulo, N.; Golderer, G.; Sailer, S.; Lackner, K.; Werner-Felmayer, G.; Liedl, K. R.; Watschinger, K. Essential role of a conserved aspartate for the enzymatic activity of plasmanylethanolamine desaturase. *Cell Mol Life Sci* **2022**, *79* (4), 214-214, DOI: 10.1007/s00018-022-04238-w

(43) Jumper, J.; Evans, R.; Pritzel, A.; Green, T.; Figurnov, M.; Ronneberger, O.; Tunyasuvunakool, K.; Bates, R.; Žídek, A.; Potapenko, A.; et al. Highly accurate protein structure prediction with AlphaFold. *Nature* **2021**, *596* (7873), 583-589, DOI: 10.1038/s41586-021-03819-2

(44) Pierre, J.-L.; Chautemps, P.; Refair, S.; Beguin, C.; El Marzouki, A.; Serratrice, G.; Saint-Aman, E.; Rey, P. Imidazolate-Bridged Dicopper(II) and Copper-Zinc Complexes of a Macrobicyclic Ligand (Cryptand). A Possible Model for the Chemistry of Cu-Zn Superoxide Dismutase. *J. Am. Chem. Soc.* **1995**, *117*, 1965-1973,

(45) Tainer, J. A.; Getzoff, E. D.; Beem, K. M.; Richardson, J. S.; Richardson, D. C. Determination and analysis of the 2 Å structure of copper, zinc superoxide dismutase. *J. Mol. Biol.* **1982**, *160* (2), 181-217, DOI: https://doi.org/10.1016/0022-2836(82)90174-7

(46) Murphy, L. M.; Strange, R. W.; Hasnain, S. S. A critical assessment of the evidence from XAFS and crystallography for the breakage of the imidazolate bridge during catalysis in CuZn superoxide dismutase. *Structure* **1997**, *5*, 371-379,

(47) López-Cabrelles, J.; Romero, J.; Abellán, G.; Giménez-Marqués, M.; Palomino, M.; Valencia, S.; Rey, F.; Mínguez Espallargas, G. Solvent-Free Synthesis of ZIFs: A Route toward the Elusive Fe(II) Analogue of ZIF-8. *J. Am. Chem. Soc* **2019**, *141* (17), 7173-7180, DOI: 10.1021/jacs.9b02686

(48) Westre, T. E.; Kennepohl, P.; DeWitt, J. G.; Hedman, B.; Hodgson, K. O.; Solomon, E. I. A Multiplet Analysis of Fe K-Edge 1s → 3d Pre-Edge Features of Iron Complexes. *J. Am. Chem. Soc.* **1997**, *119* (27), 6297-6314, DOI: 10.1021/ja964352a

(49) Chillemi, G.; Anselmi, M.; Sanna, N.; Padrin, C.; Balducci, L.; Cammarata, M.; Pace, E.; Chergui, M.; Benfatto, M. Dynamic multiple-scattering treatment of X-ray absorption: Parameterization of a new molecular dynamics force field for myoglobin. *Struct. Dyn.* **2018**, *5* (5), 054101, DOI: 10.1063/1.5031806

(50) D'Angelo, P.; Della Longa, S.; Arcovito, A.; Anselmi, M.; Di Nola, A.; Chillemi, G. Dynamic investigation of protein metal active sites: interplay of XANES and molecular dynamics simulations. *J. Am. Chem. Soc.* **2010**, *132* (42), 14901-14909, DOI: 10.1021/ja1056533

(51) Hagelueken, G.; Wiehlmann, L.; Adams, T. M.; Kolmar, H.; Heinz, D. W.; Tümmler, B.; Schubert, W.-D. Crystal structure of the electron transfer complex rubredoxin–rubredoxin reductase of Pseudomonas aeruginosa. *Proc. Acad. Nat. Sci.* **2007**, *104* (30), 12276-12281, DOI: 10.1073/pnas.0702919104

(52) Lee, H. J.; Lian, L. Y.; Scrutton, N. S. Recombinant two-iron rubredoxin of Pseudomonas oleovorans: overexpression, purification and characterization by optical, CD and 113Cd NMR spectroscopies. *Biochem. J.* **1997**, *328*, 131-136, DOI: 10.1042/bj3280131

(53) Teimoori, A.; Ahmadian, S.; Madadkar-Sobhani, A.; Bambai, B. Rubredoxin Reductase from *Alcanivorax borkumensis*: Expression and Characterization. *Biotechnol. Prog.* **2011**, *27*, 1383-1389,

(54) van Beilen, J. B.; Neuenschwander, M.; Smits, T. H. M.; Roth, C.; Balada, S. B.; Witholt, B. Rubredoxins Involved in Alkane Oxidation. *J. Bacteriol.* **2002**, *184* (6), 1722, DOI: 10.1128/JB.184.6.1722-1732.2002

(55) Williams, S. C.; Austin, R. N. An Overview of the Electron-Transfer Proteins That Activate Alkane Monooxygenase (AlkB). *Front. Microbiol.* **2022**, *13*, 845551,

(56) Katopodis, A. G. Mechanistic studies on the epoxidation system of P. oleovorans. *Ph.D. thesis, Georgia Institute of Technology* **1982**,

(57) Ravel, B.; Newville, M. ATHENA, ARTEMIS, HEPHAESTUS: data analysis for X-ray absorption spectroscopy using IFEFFIT. *J. Synchrotron Radiat.* **2005**, *12* (Pt 4), 537-541, DOI: 10.1107/s0909049505012719

(58) Delgado-Jaime, M. U.; Mewis, C. P.; Kennepohl, P. Blueprint XAS: a Matlab-based toolbox for the fitting and analysis of XAS spectra. *J. Synchrotron. Radiat.* **2010**, *17* (1), 132-137, DOI: 10.1107/s0909049509046561

(59) Rice, P.; Longden, I.; Bleasby, A. EMBOSS: The European Molecular Biology Open Software Suite. *Trends in Genetics* **2000**, *16* (6), 276-277, DOI: https://doi.org/10.1016/S0168-9525(00)02024-2

(60) Losey, N. A.; Stevenson, B. S.; Verbarg, S.; Rudd, S.; Moore, E. R. B.; Lawson, P. A. Fontimonas thermophila gen. nov., sp. nov., a moderately thermophilic bacterium isolated from a freshwater hot spring, and proposal of Solimonadaceae fam. nov. to replace Sinobacteraceae Zhou et al. 2008. *Int. J. Syst. Evol. Microbiol.* **2013**, *63* (Pt_1), 254-259, DOI: https://doi.org/10.1099/ijs.0.037127-0

(61) Dickson, C. J.; Walker, R. C.; Gould, I. R. Lipid21: Complex Lipid Membrane Simulations with AMBER. *J. Chem. Theory Comput.* **2022**, *18* (3), 1726-1736, DOI: 10.1021/acs.jctc.1c01217

(62) Maier, J. A.; Martinez, C.; Kasavajhala, K.; Wickstrom, L.; Hauser, K. E.; Simmerling, C. ff14SB: Improving the Accuracy of Protein Side Chain and Backbone Parameters from ff99SB. *J. Chem. Theory Comput.* **2015**, *11* (8), 3696-3713, DOI: 10.1021/acs.jctc.5b00255

(63) Jorgensen, W. L.; Chandrasekhar, J.; Madura, J. D.; Impey, R. W.; Klein, M. L. Comparison of simple potential functions for simulating liquid water. *J. Chem. Phys.* **1983**, *79* (2), 926-935, DOI: 10.1063/1.445869

(64) Rand, R. P.; Parsegian, V. A. Hydration forces between phospholipid bilayers. *Biochimica et Biophysica Acta (BBA) - Reviews on Biomembranes* **1989**, *988* (3), 351-376, DOI: https://doi.org/10.1016/0304-4157(89)90010-5

(65) Rappolt, M.; Hickel, A.; Bringezu, F.; Lohner, K. Mechanism of the Lamellar/Inverse Hexagonal Phase Transition Examined by High Resolution X-Ray Diffraction. *Biophys. J.* **2003**, *84* (5), 3111-3122, DOI: https://doi.org/10.1016/S0006-3495(03)70036-8

(66) Lomize, M. A.; Pogozheva, I. D.; Joo, H.; Mosberg, H. I.; Lomize, A. L. OPM database and PPM web server: resources for positioning of proteins in membranes. *Nucleic Acids Res.* **2012**, *40* (Database issue), D370-376, DOI: 10.1093/nar/gkr703

(67) Jo, S.; Kim, T.; Iyer, V. G.; Im, W. CHARMM-GUI: A web-based graphical user interface for CHARMM. *J. Comput. Chem.* **2008**, *29* (11), 1859-1865, DOI: https://doi.org/10.1002/jcc.20945

(68) Wu, E. L.; Cheng, X.; Jo, S.; Rui, H.; Song, K. C.; Dávila-Contreras, E. M.; Qi, Y.; Lee, J.; Monje-Galvan, V.; Venable, R. M.; et al. CHARMM-GUI Membrane Builder toward realistic biological membrane simulations. *J. Comput. Chem.* **2014**, *35* (27), 1997-2004, DOI: https://doi.org/10.1002/jcc.23702

(69) Anandakrishnan, R.; Aguilar, B.; Onufriev, A. V. H++ 3.0: automating pK prediction and the preparation of biomolecular structures for atomistic molecular modeling and simulations. *Nucleic Acids Res.* **2012**, *40* (Web Server issue), W537-541, DOI: 10.1093/nar/gks375

(70) Li, P.; Merz, K. M. MCPB.py: A Python Based Metal Center Parameter Builder. *J. Chem. Inf. Model.* **2016**, *56* (4), 599-604, DOI: 10.1021/acs.jcim.5b00674

(71) *Gaussian 16 Rev. C.01*; Wallingford, CT, 2016. (accessed.

(72) Lee, C.; Yang, W.; Parr, R. G. Development of the Colle-Salvetti correlation-energy formula into a functional of the electron density. *Phys Rev B Condens Matter* **1988**, *37* (2), 785-789, DOI: 10.1103/physrevb.37.785

(73) Becke, A. Density-functional thermochemistry. III. The role of exact exchange. *J. Chem. Phys* **1993**, *98*, 5648,

(74) Stephens, P. J.; Devlin, F. J.; Chabalowski, C. F.; Frisch, M. J. Ab Initio Calculation of Vibrational Absorption and Circular Dichroism Spectra Using Density Functional Force Fields. ***J. Phys. Chem.*** **1994**, *98* (45), 11623-11627, DOI: 10.1021/j100096a001

(75) Hay, P. J.; Wadt, W. R. Ab initio effective core potentials for molecular calculations. Potentials for K to Au including the outermost core orbitals. *J. Chem. Phys.* **1985**, *82* (1), 299-310, DOI: 10.1063/1.448975

(76) Ditchfield, R.; Hehre, W. J.; Pople, J. A. Self-Consistent Molecular-Orbital Methods. IX. An Extended Gaussian-Type Basis for Molecular-Orbital Studies of Organic Molecules. *J. Chem. Phys.* **1972**, *54* (2), 724-728, DOI: 10.1063/1.1674902

(77) Hariharan, P. C.; Pople, J. A. The influence of polarization functions on molecular orbital hydrogenation energies. *Theor. Chem. Acc.* **1973**, *28* (3), 213-222, DOI: 10.1007/BF00533485

(78) Hirshfeld, F. L. Bonded-atom fragments for describing molecular charge densities. *Theor. Chem. Acc.* **1977**, *44* (2), 129-138, DOI: 10.1007/BF00549096

(79) Reinhardt, C. R.; Lee, J.; Hendricks, L.; Green, T.; Kuncyznski, L.; Roberts, A.; Miller, N.; Rafalin, N.; Kulik, H. J.; Pollock, C.; et al. Moving beyond the first high-resolution structural models of alkane monooxygenase (AlkB): Active site characterization by extended X-ray absorption fine structure (EXAFS) and molecular dynamics (MD) simulations. *Zenodo* **2024**, DOI: 10.5281/zenodo.13222830

(80) Wang, J.; Wolf, R. M.; Caldwell, J. W.; Kollman, P. A.; Case, D. A. Development and testing of a general amber force field. *J. Comput. Chem.* **2004**, *25* (9), 1157-1174, DOI: https://doi.org/10.1002/jcc.20035

(81) Wang, J.; Wang, W.; Kollman, P. A.; Case, D. A. Automatic atom type and bond type perception in molecular mechanical calculations. *J. Mol. Graph. Model.* **2006**, *25* (2), 247-260, DOI: 10.1016/j.jmgm.2005.12.005

(82) Case, D. A.; Aktulga, H. M.; Belfon, K.; Ben-Shalom, I. Y.; Berryman, J. T.; Brozell, S. R.; Cerutti, D. S.; Cheatham, T. E. I.; Cisneros, G. A.; Cruzeiro, V. W. D.; et al. Amber 2023. University of California: San Francisco: 2023.

(83) Roe, D. R.; Cheatham, T. E., III. PTRAJ and CPPTRAJ: Software for Processing and Analysis of Molecular Dynamics Trajectory Data. *J. Chem. Theory Comput.* **2013**, *9* (7), 3084-3095, DOI: 10.1021/ct400341p

(84) Meng, E. C.; Goddard, T. D.; Pettersen, E. F.; Couch, G. S.; Pearson, Z. J.; Morris, J. H.; Ferrin, T. E. UCSF ChimeraX: Tools for structure building and analysis. *Prot. Sci.* **2023**, *32* (11), e4792, DOI: https://doi.org/10.1002/pro.4792

(85) Waterhouse, A. M.; Procter, J. B.; Martin, D. M. A.; Clamp, M.; Barton, G. J. Jalview Version 2—a multiple sequence alignment editor and analysis workbench. *Bioinformatics* **2009**, *25* (9), 1189-1191, DOI: 10.1093/bioinformatics/btp033

(86) Broadwater, J. A.; Haas, J. A.; Fox, B. G. The fundamental, versatile role of diiron enzymes in lipid metabolism. *Fett/Lipids* **1998**, *100*, 103-113,

(87) Jasniewski, A. J.; Que, L. Dioxygen Activation by Nonheme Diiron Enzymes: Diverse Dioxygen Adducts, High-Valent Intermediates, and Related Model Complexes. *Chem. Rev.* **2018**, *118*, 2554-2592,

(88) Kurtz, D. M. Oxo- and hydroxo-bridged diiron complexes: A chemical perspective on a biological unit. *Chem. Rev.* **1990**, *90*, 585-606,

(89) Shanklin, J.; Guy, J. E.; Mishra, G.; Lingqvist, Y. Desaturases: Emerging models for understanding functional diversification of Diiron-containing enzymes. *J. Biol. Chem.* **2009**, *284*, 18559-18563,

(90) Strange, R. W.; Blackburn, N. J.; Knowles, P. F.; Hasnain, S. S. X-ray absorption spectroscopy of metal-histidine coordination in metalloproteins. Exact simulation of the EXAFS of tetrakis(imidazole)copper(II) nitrate and other copper-imidazole complexes by the use of a multple-scattering treatment. *J. Am. Chem. Soc.* **1987**, *109*, 7157-7162,

(91) Strange, R. S.; Hasnain, S. S.; Blackburn, N. J.; Knowles, P. F. Multiple scattering in the EXAFS of imidazole containing complexes. *J. Phys. (Paris)* **1986**, *colloque C8*, CB593-596,

(92) Marlin, D. S.; Olmstead, M. M.; Mascharak, P. K. Structure−Spectroscopy Correlation in Distorted Five-Coordinate Cu(II) Complexes: A Case Study with a Set of Closely Related Copper Complexes of Pyridine-2,6-dicarboxamide Ligands. *Inorganic Chemistry* **2001**, *40* (27), 7003-7008, DOI: 10.1021/ic010523n

(93) Döhlert, P.; Irran, E.; Kretschmer, R.; Enthaler, S. Synthesis, characterization and application of iron N-substituted imidazole complexes with the motif $ClFeL_4OFeCl_3$. *Inorg. Chem. Commun.* **2015**, *51*, 4-8, DOI: https://doi.org/10.1016/j.inoche.2014.10.038

(94) Obrey, S. J.; Bott, S. G.; Barron, A. R. Molecular structure of [trans-FeCl2(imidazole)4]Cl·THF·H2O. *J. Chem. Crystallogr.* **2000**, *30* (1), 61-63, DOI: 10.1023/A:1009502317489

(95) Christie, S.; Subramanian, S.; Wang, L.; Zaworotko, M. J. Ionic liquid mediated synthesis and x-ray crystal structure of trans-difluorotetrakis- (1-methylimidazole)iron(III) tetrafluoroborate. *Inorganic Chemistry* **1993**, *32* (23), 5415-5417, DOI: 10.1021/ic00075a078

(96) Cotton, S. A.; Franckevicius, V.; Fawcett, J. Syntheses and structures of iron(III) complexes of simple N-donor ligands. *Polyhedron* **2002**, *21* (20), 2055-2061, DOI: https://doi.org/10.1016/S0277-5387(02)01137-3

(97) Wang, Y.; Liu, Y. Computational Insights into the Non-Heme Diiron Alkane Monooxygenase Enzyme AlkB: Electronic Structures, Dioxygen Activation, and Hydroxylation Mechanism of Liquid Alkanes. *Inorganic Chemistry* **2024**, DOI: 10.1021/acs.inorgchem.4c02721

(98) Zhou, S.; Wang, L. Unraveling the structural and chemical features of biological short hydrogen bonds. *Chem Sci* **2019**, *10* (33), 7734-7745, DOI: 10.1039/c9sc01496a

(99) Kemp, M. T.; Lewandowski, E. M.; Chen, Y. Low barrier hydrogen bonds in protein structure and function. *Biochim Biophys Acta Proteins Proteom* **2021**, *1869* (1), 140557, DOI: 10.1016/j.bbapap.2020.140557

For Table of Contents Use Only

alkane monooxygenase (AlkB)

EXAFS + MD Simulations = ✗ / ✓ Fe-Fe distance > 5 Å